

RESEARCH

Open Access



0-D composition and performance analysis of an air-breathing radiofrequency ion thruster

Julian Lopez-Uricoechea*, Dan Lev and Mitchell L. R. Walker

*Correspondence:
jlopezur3@gatech.edu

Georgia Institute of Technology,
School of Aerospace
Engineering, Atlanta, GA, USA

Abstract

This paper presents a physics-based 0-D steady-state model of a radiofrequency ion thruster (RIT) that is valid for any propellant blend, and hence, any plasma mixture, and the model is used to predict the drag compensation capability and plasma composition of an air-breathing RIT operating in very-low Earth orbit (VLEO). This study fills a gap in the modeling of air-breathing electric propulsion with an air-breathing RIT model that is validated with experimental data of a RIT operating with an N_2/O_2 mixture. The model expands upon current 0-D RIT models by accounting for the dissociation of neutral molecules and molecular ions and by applying particle conservation for each ion and neutral species. Atomic oxygen in the atmosphere is assumed to completely recombine into O_2 in the collector, and the model is used to calculate an air-breathing RIT's thrust, discharge efficiency, mass utilization efficiency, and discharge plasma composition at altitudes between 80 and 150 km. At 1 kW of total input power and an optimal flow rate of 0.17 mg/s, the net thrust was limited to 3 mN at all altitudes considered. At these same operating conditions, the mass utilization efficiency and discharge efficiency were approximately 0.15 and 870 eV/ion, respectively. To increase the performance of the thruster, the magnetic field should be increased in order to increase the beam current. The mole fraction of atomic oxygen in the discharge chamber was found to be between 0.19 and 0.27 depending on the altitude, indicating that grid erosion should be a focus of future studies.

Keywords: Air-breathing, Very-low Earth orbit, Radiofrequency ion thruster, Inductively coupled plasma, Multispecies plasma

Introduction

Earth observation capabilities would improve if satellites operated in VLEO, as optical imaging systems could obtain higher spatial resolutions and radar systems could achieve higher signal-to-noise ratios, among other benefits [1]. However, long-lifetime satellite missions in VLEO are currently unfeasible, and air-breathing electric propulsion (ABEP) would be the enabling technology for such missions [2]. At low altitudes, the thicker atmosphere increases the drag on the satellite and significantly accelerates the orbit decay, so a propulsion system is needed to compensate for the drag. However, for an altitude less than 250 km, the additional propellant and larger power system needed to sustain a multi-year mission would further increase the size of the spacecraft. This

in turn, would increase the drag, thereby creating a cycle that increases the amount of required propellant and the size of the power system; this cycle makes long-lifetime satellite missions in VLEO unfeasible [2]. ABEP would provide a solution by collecting the oncoming air and using the air as propellant in an electric propulsion device. This paper mainly considers electrostatic electric propulsion, in which propellant is accelerated to high velocities by an electric field [3].

The study of ABEP can be separated into three areas: the design of an intake that can efficiently collect air, the determination of whether thrusters can produce enough thrust for drag compensation while operating with an air mixture, and the analysis of the lifetime of the ABEP system. It is important to note that the surface properties of the ABEP system play a big role in the feasibility of ABEP, as the reflective properties of the intake surface directly influences the intake efficiency and plasma-surface interactions drive the surface erosion in thrusters [4]. This study relates to the latter two areas of ABEP by developing a composition model of a 1 kW gridded ion thruster that uses an inductively coupled plasma generator in the High-Power Electric Propulsion Lab (HPEPL) at Georgia Tech, and the analysis is restricted to altitudes between 80 and 150 km. Although ABEP has mostly been investigated for altitudes between 200 and 250 km, Earth observation capabilities improve at lower altitudes [1]; consequently, it is important to continue research at lower VLEO altitudes, even though operating at lower altitudes will require more input power to the thruster, as seen in Fig. 1. A key component of achieving ABEP at lower altitudes is overcoming the challenges that come with operating in a thicker atmosphere in addition to the larger drag; below 150 km, torques from aerodynamic forces make it difficult for attitude and orbit control systems to maintain a satellite at a steady altitude, and 80 km is where a satellite disintegrates during its re-entry phase. These additional challenges are, however, out of the scope of this article.

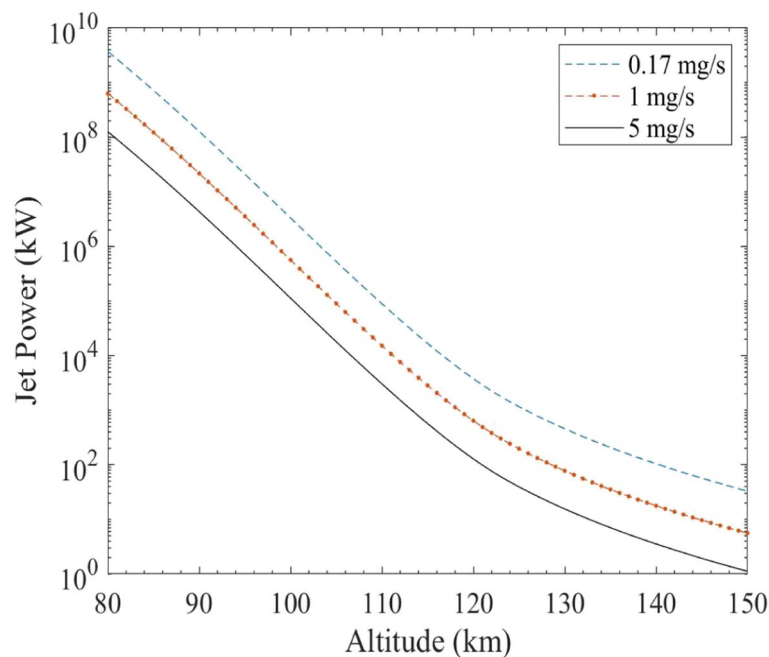


Fig. 1 Jet power required to compensate for drag in Fig. 2 at different mass flow rates through the thruster

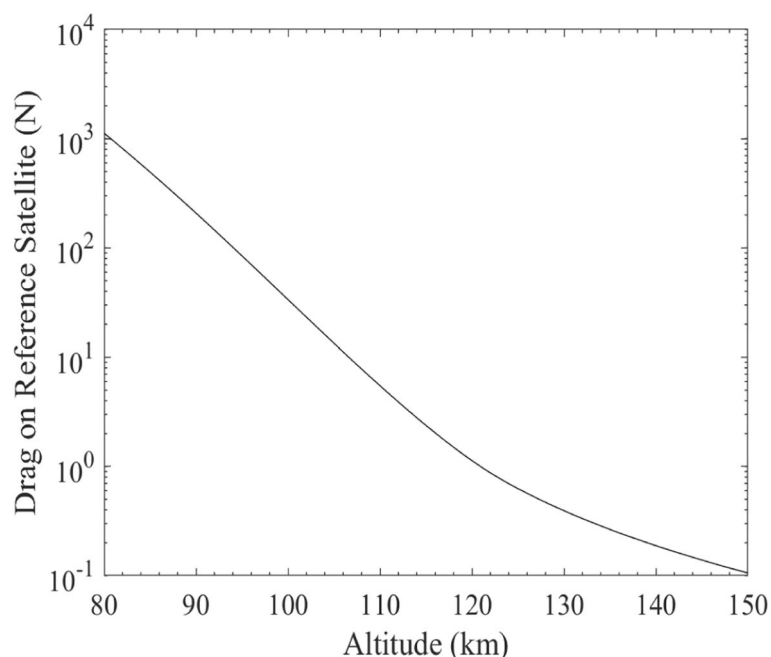


Fig. 2 Drag versus altitude for a reference satellite with a 1 m^2 cross-section and a drag coefficient of 2

The suitability for ABEP of several types of thrusters has been studied. JAXA's air-breathing ion engine (ABIE) feeds the intake flow directly into the discharge chamber, ionizes the air with an Electron Cyclotron Resonance source, and accelerates the ions through grids [5]. Although the ABIE has not been tested on an N_2/O_2 mixture, from experiments using atomic oxygen and N_2 beams to simulate the VLEO environment, the ABIE was estimated to have produced 0.13 mN of thrust using 60 W of microwave power [6]. ESA's RAM-EP device achieves the required thruster inlet pressure by stagnating the flow in the collector and uses a radiofrequency ion thruster (RIT) to provide the required thrust [7]. Experiments with an air mixture representative of 200 km using a RIT-10 EBBM have achieved thrusts between 2.25 and 7.25 mN with a total power between 180 and 520 W. Furthermore, the results suggest that the erosion-limited lifetime of the thruster could be over a year [8]. Several Hall thrusters have been tested with air mixtures [9, 10]. Hall thruster simulations suggest the feasibility of 20 mN of thrust at 1 kW of power at 250 km [11], while experiments of an ABEP system using a two-stage Hall thruster and operating on the gathered flow of a pure N_2/O_2 mixture demonstrated around 6 mN of thrust at 1100 W of total power [9]. Electrodeless thrusters are a promising technology for ABEP because they inherently avoid concerns of electrode erosion. Although experiments with a radiofrequency plasma thruster have measured that the resultant thrust was entirely due to cold gas thrust, such that RF power added no thrust [10], the Institute of Space Systems of the University of Stuttgart has been developing an air-breathing RF helicon-based inductive plasma thruster [12]. Previous ABEP work has successfully determined the performance of electric propulsion devices on N_2/O_2 mixtures, but to increase the performance of these devices, it is necessary to improve the understanding of the ionization and acceleration of N_2/O_2 mixtures.

While models have been presented for analysis of air-breathing Hall thrusters [11, 13], a model has not been presented for an air-breathing RIT. The main benefits of a RIT are the electrodeless discharge chamber and the well-understood acceleration grids. However, grid erosion with an air mixture needs to be characterized to determine the suitability of a RIT for ABEP. Two different 0-D models of a RIT operating on monatomic propellants have been presented by Goebel [14] and Chabert et al. [15]. Goebel assumes ambipolar diffusion across the axial magnetic field but does not calculate the magnetic field strength nor the power absorbed by the plasma. In contrast, Chabert presents a model of a cylindrical inductively coupled plasma (ICP) that can be used to calculate the magnetic field strength and the power absorbed by the plasma, but Chabert's 0-D model does not include the effect of the magnetic field strength.

The goal of this study was to develop a composition model of an air-breathing RIT to analyze the suitability for ABEP of a RIT that uses the ICP generator at HPEPL; in this study, the suitability of the thruster at a given altitude is quantified by the percent of drag on a satellite with a 1 m² frontal area and drag coefficient of 2 that is compensated by a 1 kW RIT. The composition model in this paper combines the 0-D discharge chamber model of Goebel and the 0-D ICP model of Chabert and generalizes the combined model for a plasma of an N₂/O₂ mixture. [Analytical model](#) section presents the air-breathing RIT model by formulating the necessary equations for ion conservation, neutral particle conservation, and energy conservation. In [Verification of model](#) section, the model is validated against experimental data from [8] of a RIT-10 operating on an N₂/O₂ mixture and on just N₂ or O₂. The model agrees well with experimental data at low mass flow rates and follows the general trends seen in the data. The power of the model is demonstrated in [Results and discussion](#) section, where the predicted performance and discharge plasma composition are presented for an air-breathing RIT that uses the ICP generator from HPEPL. The relevance of the results regarding thruster efficiency and system-level drag compensation are discussed.

Analytical model

A 0-D model of a cylindrical inductively coupled plasma is developed for a 13-species model of an air plasma. The 13 species considered are e^- , N₂, N₂⁺, N₂⁺⁺, N, N⁺, N⁺⁺, O₂, O₂⁺, O₂⁺⁺, O, O⁺, and O⁺⁺. [Atmospheric model](#) section presents the atmospheric model used to calculate the composition at the intake. In [Collision rates](#) section, the types of collisions used in the model are introduced, and the ion and neutral production rates are formulated. [Ion conservation](#), [Neutral particle conservation](#), and [Energy conservation](#) sections establish the equations used for ion conservation, neutral particle conservation, and energy conservation, respectively. The terms used in the conservation equations are shown in the schematic of the discharge chamber in Fig. 3. [Model of ICP](#) section summarizes Chabert's ICP model, and the performance model in [Performance model](#) section presents how the model of the discharge chamber is used to calculate the thrust and thruster input power. [Model implementation](#) section then discusses how the presented model is used to calculate the plasma parameters and how the model was implemented in this study.

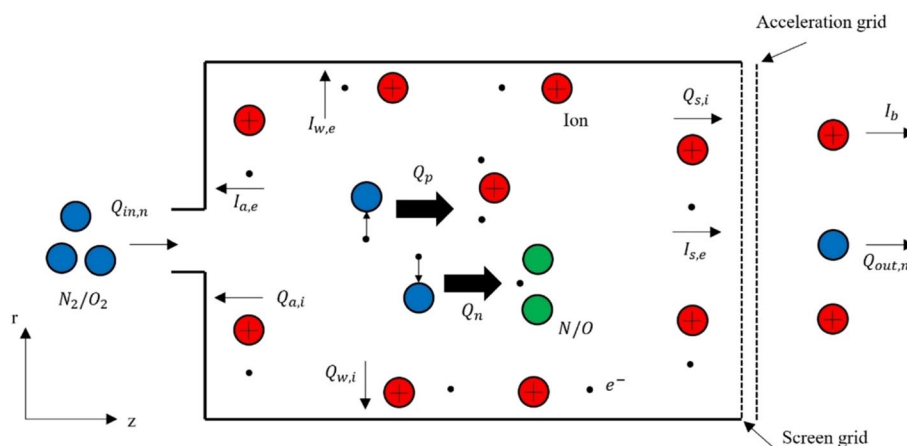


Fig. 3 Schematic of particle fluxes and source terms in the 0-D model. $Q_{s,i}$, $Q_{a,i}$, and $Q_{w,i}$ refer to the ion flux to the screen grid, back wall, and radial wall, respectively. $I_{s,e}$, $I_{a,e}$, and $I_{w,e}$ refer to the electron current to the screen grid, back wall, and radial wall, respectively. Q_p and Q_n are the production rates of ions and neutrals, respectively. I_b is the beam current, and $Q_{in,n}$ and $Q_{out,n}$ are the particle fluxes of neutrals at the inlet and through the grids, respectively

The 0-D model of the steady-state discharge is adapted for an arbitrary plasma mixture from Goebel, using the ICP model of Chabert. The model assumes that all the discharge chamber walls are floating and that the wall temperature is 500 K. For a plasma mixture, there is no closed-form solution for the plasma properties, so, for the species considered, a system of 15 equations is developed for the steady-state solution of the plasma properties. The plasma properties are the densities of the 13 species, the electron temperature, and the floating sheath potential. There are 13 equations between ion conservation, neutral particle conservation, and quasi-neutrality, while energy conservation and ambipolarity are also maintained. The necessary total power can be solved for at a given thrust requirement and beam voltage. It is important to note that while being a key component of the feasibility of ABEP, the neutralizer cathode is not included in the analysis in this study. In fact, cathode operation on an N_2/O_2 mixture is an active area of research as oxygen significantly reduces the lifetime of thermionic cathodes, so the feasibility of field emission cathodes and of microwave cathodes is being explored [16].

While the air intake is not analyzed in this paper, Diamant [17] has suggested that an air-breathing Hall thruster requires that the intake flow be stagnated. While Diamant’s study focused on a Hall thruster, the same conclusion applies to a RIT since a higher pressure would increase the ionization rates in the discharge chamber, and a lower neutral velocity would decrease the neutral flux through the grids. ESA’s proposed RAM-EP system, which uses a RIT, stagnates the flow. Singh [16] suggests that in the collection process, the atomic oxygen recombines into O_2 . As a result, in this model, it is assumed that the intake flow is stagnated and that all the oxygen that enters the discharge chamber is O_2 .

Atmospheric model

The NRLMSISE-00 atmospheric model [18] is used to calculate the densities of N_2 , O_2 , and O as a function of altitude and solar activity. The altitude range considered is 80 to 150 km, and the solar activities considered are low, moderate, and high, where the reference values of the daily F10.7 and the average F10.7 for each level of solar activity are taken from [19].

The intake is not analyzed in this article, so instead of calculating the mass flow rate at the intake using the intake area, the mass flow rate at the intake outlet is an input of the model. The performance of the thruster at various altitudes at a given mass flow rate is then dependent on how the mole fractions of N_2 , O_2 , and O change with altitude. More specifically, the intake mass flow rate and the mole fractions of N_2 , O_2 , and O at an altitude will dictate the neutral fluxes of each species at the thruster inlet. Assuming the recombination of atomic oxygen in the collection process, the mole fractions of N_2 and O_2 at the thruster inlet are shown as a function of altitude in Fig. 4. The atmospheric density, which is proportional to the intake mass flow rate, is shown as a function of altitude at different levels of solar activity in Fig. 10.

Collision rates

The types of collisions rates considered are the following: electron impact ionization rates of neutrals and singly-charged ions, electron impact excitation rates of neutrals, neutral-neutral and ion-neutral recombination rates, and electron-neutral and electron-ion elastic momentum-transfer collision rates. The dominant electron-ion recombination event in an air plasma is dissociative recombination [20]; however, at the electron temperatures and low ionization fractions delivered by the model, the contribution of the dissociative recombination rates from [20] to the net production rates is negligible compared to that

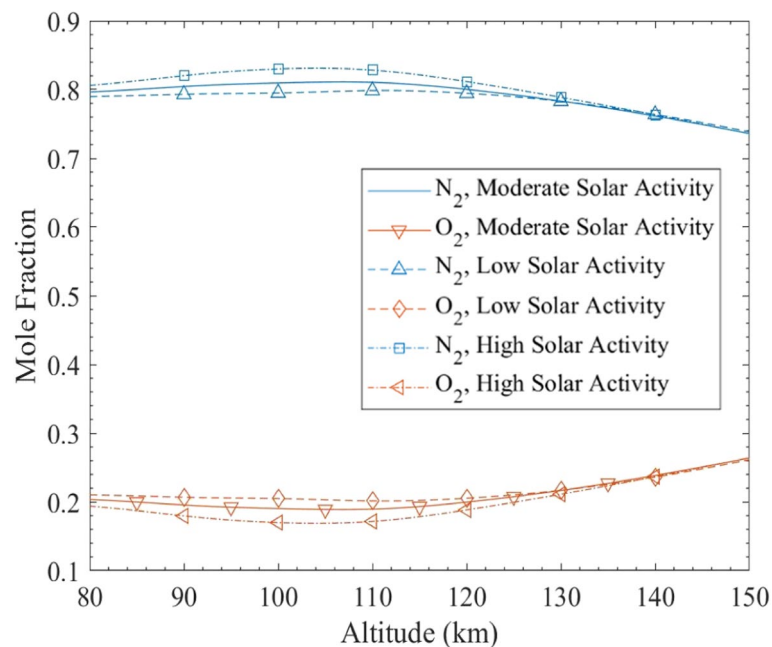


Fig. 4 Mole fractions at the thruster inlet as a function of altitude with varying level of solar activity

of electron impact dissociation rates used in this article. As a result, the reverse processes of the electron impact collisions can be neglected. Similarly, for the choice of ion-neutral temperature in this model, it is assumed that the neutral-neutral and ion-neutral dissociation reactions are negligible. It was found that, at the intake mass flow rates considered in this model and at the electron temperatures delivered by the model, the neutral-neutral and ion-neutral reaction rates from [20] were negligible compared to the electron impact rates. It is also assumed that at the range of electron temperature considered in this model, losses due to vibrational and rotational excitation are negligible compared to losses from electronic excitation. From Itikawa [21, 22], the dominant rotational excitations of N_2 and O_2 have excitation energies of 1.48×10^{-3} eV and 1.78×10^{-3} eV, respectively, while the vibrational energy levels of N_2 and O_2 are separated by 0.289 eV and 0.214 eV, respectively; Itikawa also shows that the electron impact cross-section for rotational and vibrational excitation of N_2 and O_2 are of the same order of magnitude as their respective ionization and excitation cross-sections, justifying the aforementioned assumption. Charge exchange collisions in the discharge chamber are also neglected. The collisional processes considered and the references for the associated cross-section data are shown in Table 1. Unless otherwise noted, the threshold energy for a particular electron impact collision is taken from the same source that contains the cross-sections.

Table 1 Electron impact collisions considered and references used for collision cross-section

Collision Type	Reaction	Reference
Ionization	$N_2 + e^- \rightarrow N_2^+ + 2e^-$	[21]
Ionization	$O_2 + e^- \rightarrow O_2^+ + 2e^-$	[23]
Ionization	$N + e^- \rightarrow N^+ + 2e^-$	[24]
Ionization	$O + e^- \rightarrow O^+ + 2e^-$	[25]
Ionization	$N^+ + e^- \rightarrow N^{++} + 2e^-$	[26]
Ionization	$O^+ + e^- \rightarrow O^{++} + 2e^-$	[27]
Ionization and Dissociation	$N_2 + e^- \rightarrow N^+ + N + 2e^-$	[21]
Ionization and Dissociation	$O_2 + e^- \rightarrow O^+ + O + 2e^-$	[23]
Ionization	$N_2^+ + e^- \rightarrow N_2^{++} + 2e^-$	[28]
Ionization	$O_2^+ + e^- \rightarrow O_2^{++} + 2e^-$	[29]
Ionization and Dissociation	$N_2^+ + e^- \rightarrow N^+ + N^+ + 2e^-$	[28]
Ionization and Dissociation	$O_2^+ + e^- \rightarrow O^+ + O^+ + 2e^-$	[29]
Electronic Excitation	$N_2 + e^- \rightarrow N_2^* + e^-$	[21]
Electronic Excitation	$O_2 + e^- \rightarrow O_2^* + e^-$	[30]
Electronic Excitation	$N + e^- \rightarrow N^* + e^-$	[31]
Electronic Excitation	$O + e^- \rightarrow O^* + e^-$	[25]
Dissociation	$N_2 + e^- \rightarrow 2N + e^-$	[32]
Dissociation	$O_2 + e^- \rightarrow 2O + e^-$	[30, 33] ^a
Dissociation	$N_2^+ + e^- \rightarrow N^+ + N + e^-$	[28]
Dissociation	$O_2^+ + e^- \rightarrow O^+ + O + e^-$	[29]
Electron- N_2 elastic momentum transfer	–	[21]
Electron- O_2 elastic momentum transfer	–	[22]
Electron-N elastic momentum transfer	–	[34]
Electron-O elastic momentum transfer	–	[29]

^a Collision cross-section data is taken from [30], and threshold energies of different dissociation channels are taken from [33]

For the electron-neutral elastic collision rates and all the inelastic electron impact rates, the collision cross-section data were found as a function of electron energy in [21–32, 34], and the collision rates were calculated by numerically evaluating

$$K_{ej}^{xp} = \int_0^{\infty} \sigma_j^{xp} \left(\frac{1}{2} m_e v_e^2 \right) v_e f(v_e) dv_e \quad (1)$$

where x represents the collision type, p represents the product, and $f(v_e)$ is the Maxwell-Boltzmann speed distribution of the electrons at a specified electron temperature. The accuracy of the numerical integration of Eq. 1 is dependent on the tail of the collision cross-section data; while most collision cross-section data cover the range up to 200 eV, 11 out of 106 datasets only went up to 50 eV, and one only went up to 40 eV. However, over the range of mass flow rates considered, the electron temperature outputted by the model did not exceed 15 eV, which, combined with the fact that all the smaller datasets had low-energy tails, suggests that the numerical error when calculating Eq. 1 is negligible. It should be noted that this could be a source of error over a greater range of mass flow rates that results in higher electron temperatures. An example of the numerical integration is shown in Fig. 5.

Because there is no localized electron source in an ICP and because of the heating mechanism in an ICP, 0-D models are appropriate for RIT's [14]. Assuming uniform density distributions and no temperature gradients in the discharge chamber, the electron impact rate in the discharge chamber for the j^{th} collision channel is

$$Q_{ej}^{xp} = V n_e n_j K_{ej}^{xp} \quad (2)$$

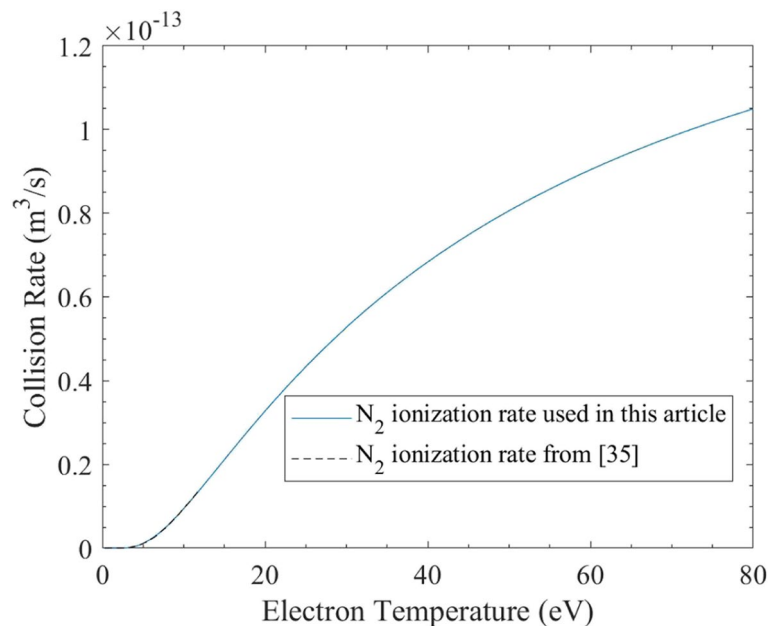


Fig. 5 Collision rate of electron impact ionization of N_2 used in model and presented by Vojnovic et al. [35]

where n_j is the source particle density. The net production rate of the j^{th} ion species is then

$$Q_{p,j} = \sum_k Q_{ek}^j - \sum_m Q_{ei_j}^{x_m} \quad (3)$$

where the first term represents summation over all the ionization channels that result in the j^{th} ion, and the second term represents summation over all the electron impact channels with the j^{th} ion as the source. Similarly, the net production rate from collisions of the k^{th} neutral species is

$$Q_{n,k} = \sum_j Q_{ej}^{D_k} - \sum_m Q_{en_k}^{x_m} \quad (4)$$

where the first term represents summation over all the electron impact dissociation channels that results in the k^{th} neutral, and the second term represents summation over all the electron impact channels with the k^{th} neutral as the source.

The total electron elastic momentum-transfer collision frequency is defined as

$$\nu_m = \sum_j n_{i,j} K_{ei_j}^{el} + \sum_k n_{n,k} K_{en_k}^{el} \quad (5)$$

where the first term represents the total electron-ion momentum-transfer collision frequency, and the second term represents the total electron-neutral momentum-transfer collision frequency. Differential cross-sections for the inelastic collisions considered in this model are not well reported. However, from [36], the total momentum-transfer cross-section of N_2 is well approximated by just the elastic momentum transfer, so for the model, the inelastic momentum transfer of all molecules is neglected. The electron-ion elastic collisions are defined using the coulomb cross section [37], such that the electron-ion elastic momentum-transfer collision rate for a specific ion species is

$$K_{ei_j}^{el} = \frac{4}{3} \left(\frac{eq_j}{4\pi\epsilon_0} \right)^2 \frac{\sqrt{2\pi}}{m_e^{1/2} (k_B T_e)^{3/2}} \ln \Lambda_j \quad (6)$$

where the Coulomb logarithm for a given ion species is given by

$$\ln \Lambda_j = \ln \left(\frac{12\pi (\epsilon_0 k_B T_e)^{3/2}}{n_e^{1/2} e^2 q_j} \right). \quad (7)$$

Ion conservation

For ion conservation of a given ion species and assuming that there is no net accumulation of ions in the plasma, the corresponding ion loss and ion production rates need to be equal, such that

$$Q_{i,j} = Q_{p,j} \quad (8)$$

where $Q_{p,j}$ is taken from Eq. 3. In addition to producing the ion beam, ions are assumed to neutralize at the radial wall, screen, and back wall. The ion loss rate is thus equal to the sum of ion loss at the radial wall, screen, and back wall and the beam ion flux, such that

$$Q_{i,j} = Q_{s,j} + Q_{a,j} + Q_{w,j} + Q_{b,j} \quad (9)$$

The ions leave the plasma in the axial direction with the Bohm flux density given by

$$J_{B,j} = h_L n_{i,j} v_{B,j} \quad (10)$$

where $h_L = 0.5$ is the planar edge-to-center density ratio assuming that the mean free path of ion-neutral collisions is significantly larger than the length of the discharge chamber [38]. For a specific ion species, the Bohm velocity is given by

$$v_{B,j} = \sqrt{\frac{k_B T_e q_j}{m_{i,j} e}}. \quad (11)$$

The ion losses at the screen and back wall and in the beam are then given by

$$Q_{s,j} = J_{B,j} A_g (1 - T_g) \quad (12)$$

$$Q_{a,j} = J_{B,j} A_a \quad (13)$$

$$Q_{b,j} = J_{B,j} A_g T_g. \quad (14)$$

The proposed thruster does not yet have designed acceleration grids, so space-charge limited current is not calculated in this model. As a result, the Bohm flux density is used in calculating the ion flux in the beam, and the beam current is calculated by

$$I_b = \sum_j q_j Q_{b,j}. \quad (15)$$

The ion loss at the radial wall in the presence of the axial magnetic field is calculated assuming ambipolar diffusion across the magnetic field [14]. The ion loss at the radial wall is then given by

$$Q_{w,j} = h_R n_{i,j} v_{B,j} f_{c,j} A_w \quad (16)$$

where $h_R = 0.4$ is the radial edge-to-center density ratio assuming that the mean free path of ion-neutral collisions is significantly larger than the radius of the discharge chamber [38]. The derivation of the ion confinement factor for the different ion species is outlined in the [Appendix](#). This derivation is a key component for extending previous 0-D RIT models [14] for propellant mixtures or molecular propellants.

Charge neutrality is assumed, such that

$$en_e = \sum_j q_j n_{i,j}. \quad (17)$$

Neutral particle conservation

For neutral particle conservation of each species in the discharge chamber, the sum of particle flux in and the net neutral production is equated to the particle flux out, such that

$$Q_{in,k} + Q_{prod,k} = Q_{out,k} \quad (18)$$

The particle flux into the discharge chamber is related to the particle flux into the collector, given by

$$Q_{0,k} = \frac{x_{i,k} \dot{m}_0}{m_{n,k}} \quad (19)$$

where the neutral mole fractions at the collector inlet are obtained as a function of altitude using the atmosphere model described in [Atmospheric model](#) section. Assuming that no air is stored by the collector, $Q_{in,N_2} = Q_{0,N_2}$, and assuming that the atomic oxygen recombines in the collector, $Q_{in,O_2} = Q_{0,O_2} + \frac{1}{2}Q_{0,O}$. For all other species, $Q_{in,k} = 0$. The net neutral production is adapted from the formulation in [15]; since ions are neutralized at the discharge chamber walls, the net neutral production is then the sum of the net neutral production rate from collisions between particles and the ion loss rate at the discharge chamber walls, such that

$$Q_{prod,k} = Q_{n,k} + \sum_j Q_{s,j} + Q_{a,j} + Q_{w,j} \quad (20)$$

where $Q_{n,k}$ is defined as in Eq. 4, and the summation is over all ionized forms of the neutral species. The particle flux out of the discharge chamber is given by kinetic theory, such that

$$Q_{out,k} = \frac{1}{4} n_{n,k} v_{n,k} A_g T_{g,n} \eta_c. \quad (21)$$

Energy conservation

For energy conservation, the power lost by the plasma is equated to the power absorbed by the plasma, such that

$$P_{loss} = P_{abs}. \quad (22)$$

The power lost by the plasma is adapted from the formulation used by [14]. For a mixture and assuming that all the surfaces float, the power lost by the plasma is given by

$$P_{loss} = \sum_{k,p,x} e Q_{ek}^{x_p} U_{ek}^{x_p} + \sum_j q_j Q_{ij} \left(2.5 \frac{k_B T_e}{e} + \Phi \right) \quad (23)$$

where the first term represents the electron energy loss from all inelastic collisions, and the second term represents the summation over all ion species for the ion and electron energy loss across the floating sheath potential at the discharge chamber boundaries.

The floating sheath potential is found by assuming ambipolarity and equating the total ion current and the total electron current. The ion and electron currents at the radial wall cancel out, such that the sheath potential is found by Eq. 24.

$$I_{a,e} + I_{s,e} = \sum_j q_j Q_{a,j} + \sum_j q_j Q_{s,j} + \sum_j q_j Q_{b,j}. \quad (24)$$

where the electron current at the screen and at the back wall are given by [14]

$$I_{s,e} = \frac{1}{4} n_e e \sqrt{\frac{8k_B T_e}{\pi m_e}} \exp\left(-\frac{e\Phi}{k_B T_e}\right) A_g (1 - T_g) \quad (25)$$

$$I_{a,e} = \frac{1}{4} n_e e \sqrt{\frac{8k_B T_e}{\pi m_e}} \exp\left(-\frac{e\Phi}{k_B T_e}\right) A_a. \quad (26)$$

Model of ICP

The discharge chamber is modeled as a system composed of the coil, discharge chamber walls, and plasma. The RF current flowing in the walls is negligible, so the power from the RF power generator is dissipated into the coil and the plasma. The model presented is taken from [15]. Neglecting the end effects of the electromagnetic field produced by the solenoid and assuming uniform electron density, the time-averaged quantities of current through the coil and power absorbed by the plasma are related to the input RF power by

$$I_{coil} = \sqrt{\frac{2P_{RF}}{(R_{coil} + R_{ind})}} \quad (27)$$

$$P_{abs} = \frac{R_{ind}}{R_{coil} + R_{ind}} P_{RF}. \quad (28)$$

R_{coil} is theoretically determined by the resistivity of the coil material, the dimensions of the coil, and by accounting for the skin effect.

By applying Poynting's theorem to the time-varying electromagnetic fields produced by the coil, the resistive component of the complex impedance of the system is found to be

$$R_{ind} = \frac{2\pi N^2}{L\omega\epsilon_0} \text{Re} \left[\frac{ikR J_1(kR)}{\epsilon_p J_0(kR)} \right] \quad (29)$$

where J_0 and J_1 are Bessel functions and where $k = k_0 \sqrt{\epsilon_p}$, with $k_0 = \omega/c$. Because the electron density is uniform in the discharge chamber, the complex permittivity of the plasma is also uniform, and assuming negligible ion and neutral velocity compared to electron velocity and negligible inelastic momentum transfer, the plasma permittivity is given by

$$\epsilon_p = 1 - \frac{\omega_{pe}^2}{\omega(\omega - i\nu_m)} \quad (30)$$

where the electron plasma frequency is given by

$$\omega_{pe} = \sqrt{\frac{n_e e^2}{m_e \epsilon_0}}. \quad (31)$$

The time-averaged axial magnetic field, which is used to calculate the ion confinement factors, is given by the expression for an infinitely long coil,

$$B = \frac{\mu_0 N I_{coil}}{L}. \quad (32)$$

Because of the aspect ratio of the coil in the proposed RIT described in Table 2, Eq. 32 is appropriate for the analysis in this paper.

Performance model

Once the plasma parameters are calculated, the performance of the thruster is evaluated. Because there is no propellant limitation, the main performance parameters are the thrust and total input power.

Accounting for the inlet mass flow rate of air at the intake, the thrust produced by a mixture of ions is given by

$$\tau = \sum_j \tau_j - \dot{m}_0 v_0 \quad (33)$$

where the orbital velocity of the satellite at a given altitude is obtained assuming a circular orbit, and the thrust due to a certain ion is

$$\tau_j = \dot{m}_{i,j} v_{i,j}. \quad (34)$$

From the conservation of energy and assuming the collected air is stagnated, the exhaust velocity for a given ion species in a gridded ion thruster is given by

$$v_{i,j} = \sqrt{\frac{2q_j \left(V_b + \Phi + \frac{k_B T_e}{2e} \right)}{m_{i,j}}} \quad (35)$$

where $V_b + \Phi + \frac{k_B T_e}{2e}$ is the net voltage through which an ion is accelerated. The mass flow rate of a given ion species is

$$\dot{m}_{i,j} = Q_{b,j} m_{i,j}. \quad (36)$$

Alternatively, for a given thrust and beam voltage, the solver of the plasma parameters can be constrained using Eq. 33, and the required RF power will be the additional output. The total input power for the thruster is defined as

Table 2 Input parameters of air-breathing RIT

L	R	N	ω	R_{coil}	$T_{g,n}$	T_g	η_c
25.4 cm	2.54 cm	3	13.56 MHz	0.2 Ω	0.62	0.85	0.6

$$P_{in} = P_{RF} + I_b V_b \tag{37}$$

where it is noted that the power required for the neutralizer cathode is not included in this analysis.

Model implementation

The system of equations used for solving for the plasma parameters is Eqs. 8, 17, 18, 22, and 24, where forms of Eqs. 8 and 18 are used for each ion and neutral, respectively. As previously noted, for a given thrust and beam voltage, Eq. 33 is added to the system of equations, and the total input power is the additional output.

The model of the RIT was used to analyze the performance and plasma composition of an air-breathing thruster using an RF ion source built in HPEPL. The thruster parameters assumed for the air-breathing RIT are shown in Table 2; the RF ion source in HPEPL had a measured coil resistance of around 0.2 Ω. It should be noted that the parameters for the ion optics are only for the model and do not represent calculated ion optics performance for an air-breathing RIT.

The model was implemented at altitudes between 80 and 150 km and at beam voltages of 1000 V, 1500 V, 2000 V, 2500 V, and 3000 V. All cases have the same mass flow rate range at the intake. The effect of solar activity was analyzed by assuming that the intake is designed for moderate solar activity and by considering what design mass flow rate is needed for the actual mass flow rate.

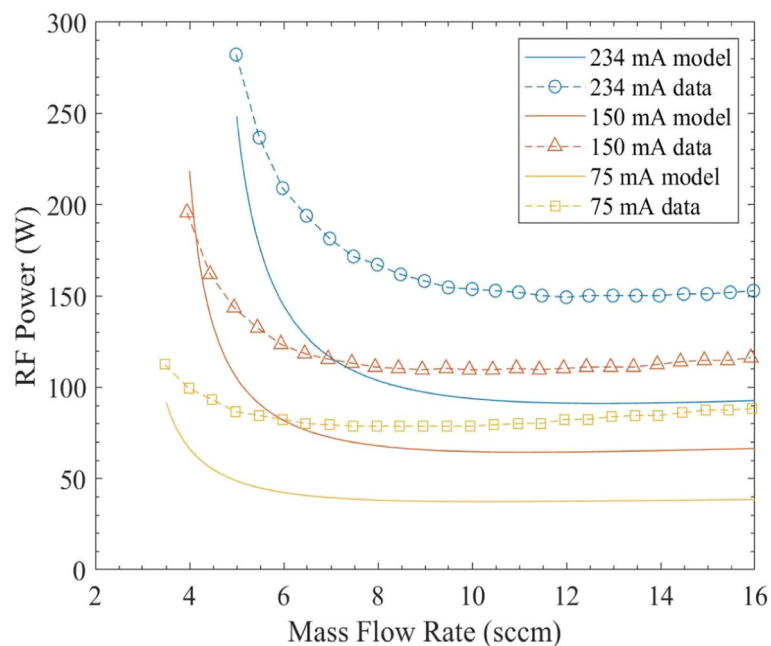


Fig. 6 Comparison of model and experimental data for RF power as a function of mass flow rate on constant beam current lines with an N₂/O₂ mixture. Uses experimental data from [8]

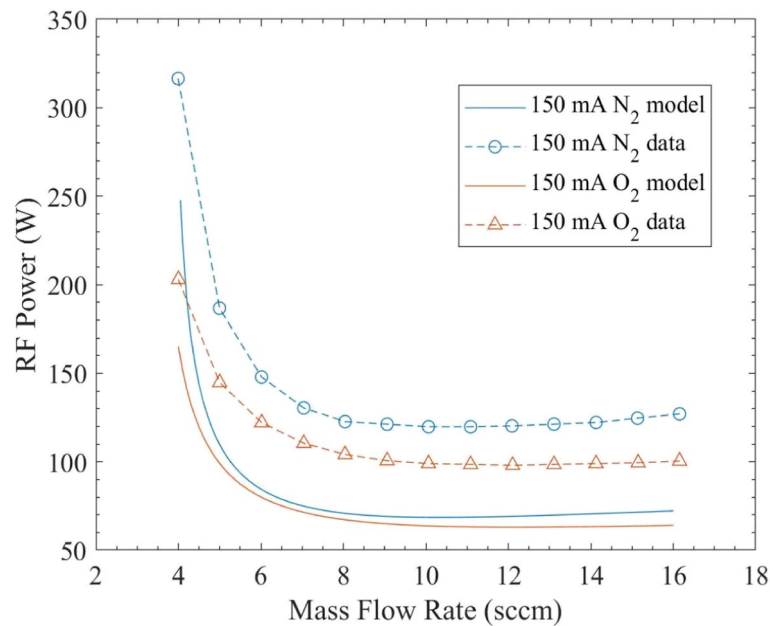


Fig. 7 Comparison of model and experimental data for RF power as function of mass flow rate on constant beam current lines with N_2 and O_2 propellant. Uses experimental data from [8]

Verification of model

The model of the RIT was compared with existing data of the RIT-10 EBBM thruster operating with an N_2/O_2 mixture and with just N_2 or O_2 propellant [8]. A beam plasma potential of 20 V was assumed to convert the N_2/O_2 mixture data from total power to RF power.

The results from the presented RIT model and the experimental data are shown in Figs. 6 and 7. At a beam current of 234 mA, the model captures the hyperbolic shape of the curve seen in the experimental data, but at the lower beam currents, the model does not capture the linear increase in RF power at the higher mass flow rates. Specifically, the model can approximately predict the mass flow rates at the inflection points of the curves and the mass flow rates to which the curves asymptote; it is important to note that the latter prediction indicates that the model can accurately predict the composition in the discharge chamber since the degree of dissociation determines the beam current for a discharge chamber with 100% mass utilization efficiency. At higher mass flow rates, the discrepancy between the model and the experimental data is approximately constant across the different beam currents at around 50 W; the high mass flow regions have approximately constant predicted RF powers, so an approximately constant discrepancy in power is expected. Lastly, the model generally underpredicts the required RF power, which is to be expected since the model does not account for any operational energy losses present during the experiment, such as losses due to do impedance mismatches.

Results and discussion

The thruster's performance and the discharge plasma composition are analyzed at various VLEO altitudes using the framework in [Analytical model](#) section. The analysis shows how the performance and plasma composition vary with altitude, intake mass flow rate,

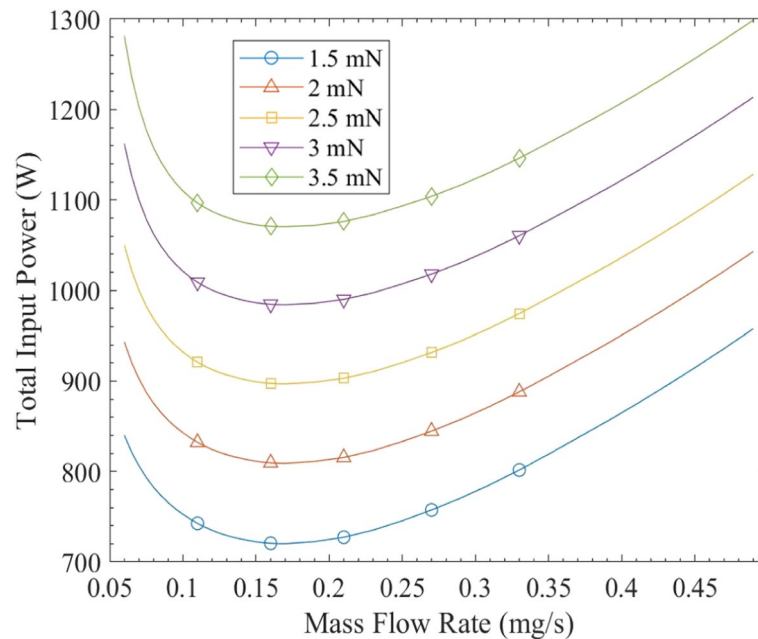


Fig. 8 Total power versus mass flow rate at constant thrust of 1.5 mN, 2 mN, 2.5 mN, 3 mN, and 3.5 mN. Results calculated at 150 km with moderate solar activity

and beam voltage. It was seen that the highest performance is achieved with a beam voltage between 2000 and 3000 V. Of the test cases, a beam voltage of 2500 V achieved the highest performance, so the results shown are all calculated with a beam voltage of 2500 V.

Figure 8 exhibits the expected hyperbolic behavior of the required power at lower mass flow rates, which is a trend that corresponds to an increasing mass utilization efficiency, but because of the inclusion of the intake drag in the net thrust, the required power increases linearly for higher mass flow rates. The performance curves presented are in terms of the mass flow rates, which include the ambient densities and intake area, and Fig. 4 shows that the inlet composition does not vary significantly in the altitude range considered. As a result, it was observed that the altitude has a negligible effect on the thruster's performance; as expected, the higher orbital velocity produces more drag at lower altitudes, which slightly increases the required power for a given net thrust. This effect increases as the mass flow rate increases. Figure 8 shows that at 150 km, if constrained to 1 kW of total power, then the maximum amount of net thrust is approximately 3 mN. Although operating at a higher power than experiments performed by [8], the thrust is within the values achieved by [8] using a RIT-10 on an N_2/O_2 mixture. Also, with the grid spacing of the mass flow rate input values used, there is no variation in the optimal mass flow rate for different values of thrust, and the optimal value for the mass flow rate is 0.17 mg/s.

Because of the negligible change in the optimal mass flow rate in the constant thrust curves, to increase the thrust at a given altitude, more input power is needed, and the same intake should be used. Also, because the maximum net thrust for 1 kW of total input power is approximately 3 mN at all altitudes considered, the presented design of an air-breathing RIT is significantly more competitive at higher altitudes. Assuming a

satellite with a drag coefficient of 2 and a 1 m^2 frontal area and with a moderate level of solar activity, the 3 mN of thrust compensates for 2.85%, 0.266%, and 0.00027% of the drag at 150 km, 120 km, and 80 km, respectively. To achieve the target mass flow rate of 0.17 mg/s assuming a moderate level of solar activity, circular orbits, and 100% collector efficiency at the intake, the required intake areas would be 126 cm^2 , 11.8 cm^2 , and 0.0119 cm^2 at 150 km, 120 km, and 80 km, respectively. The low percentages of drag compensation suggest that the presented thruster is not well suited for complete drag compensation. Further analysis is needed to determine the suitability of the presented thruster for partial drag compensation; from Fig. 1, it is evident that a 1 kW thruster operating at 0.17 mg/s cannot compensate for the drag of the reference satellite at 150 km. However, a larger RIT could operate efficiently at higher mass flow rates and thus compensate for a larger portion of the drag at a given jet power, so the size of the RIT should be a focus of future studies. It should also be noted that a satellite should ideally be almost entirely behind the intake to maximize the drag compensation, but the required intake areas are all more than fifty times smaller than the frontal area of the reference satellite. If a satellite frontal area of 200 cm^2 is chosen, such that the required intake area at 150 km is around 39% of the total frontal area, then the 3 mN of net thrust would compensate for 142.5% of the drag on the satellite at 150 km. The previous suggestion of using a larger RIT would also increase the percentage of the required intake area among the total frontal area, but further investigation is required to determine the optimal flow rates for larger RIT's.

Although Fig. 8 does not account for the space-charge limit, the results provide valuable insight into the air-breathing RIT's required grid spacing. First, it is necessary to consider the thrust from the ion beam instead of the net thrust. Considering the optimal operating condition of 0.17 mg/s mass flow rate at the intake and assuming a circular

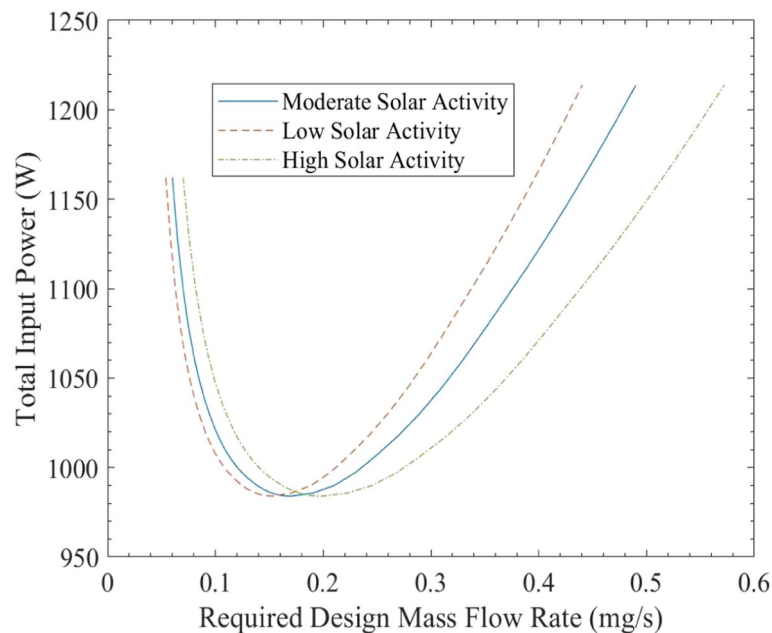


Fig. 9 Total power versus design mass flow rate at constant thrust of 3 mN with varying level of solar activity. Results calculated at 150 km

orbit, the drag on the intake is approximately 1.3 mN at all altitudes between 80 and 150 km. The corresponding ion thrust when maximizing the net thrust at 1 kW of total power is then 4.3 mN. At a given total acceleration voltage, the required grid spacing to achieve 4.3 mN of space-charge limited thrust could then be calculated.

Figure 9 shows the total input power required to maintain 3 mN of thrust as a function of the required design mass flow rate. When the intake is designed for the optimal mass flow rate at a moderate solar activity, the power requirement for 3 mN of net thrust at low or high levels of solar activity is less than 1% larger than that at moderate solar activity. If the same curves were plotted against the actual mass flow rate at the intake rather than the mass flow rate of the design intake that would result in the actual mass flow rate at the corresponding level of solar activity, then the curves would overlap almost exactly with a negligible difference. This was also the case at 100 km, which has more composition variation than 150 km, as seen in Fig. 4. The effect of solar activity on the thruster's performance is almost entirely from the change in density and not from the change in composition. This finding is consistent with the atmosphere's composition shown in Figs. 4 and 10, since in Fig. 4, the mole fractions only change by at most 0.05 with solar activity, while the design mass flow rate is proportional to density, which can vary by 20% with solar activity, as seen in Fig. 10. As a result, solar activity has a larger impact on thruster performance at higher altitudes.

During in-flight operation, the ambient density will also vary as the spacecraft's altitude decreases during shadow phases and increases when making up for the lost altitude. For a fixed intake area, this will result in a variation in the mass flow rate greater than that seen with a change in the level of solar activity. For example, for a target altitude of 150 km with an intake designed for a mass flow rate of 0.17 mg/s

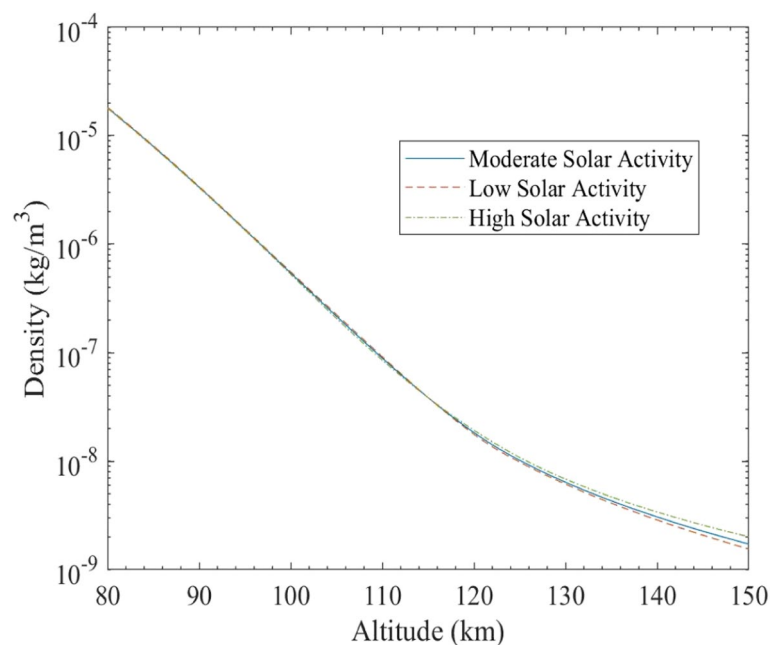


Fig. 10 Air density as a function of altitude with varying level of solar activity

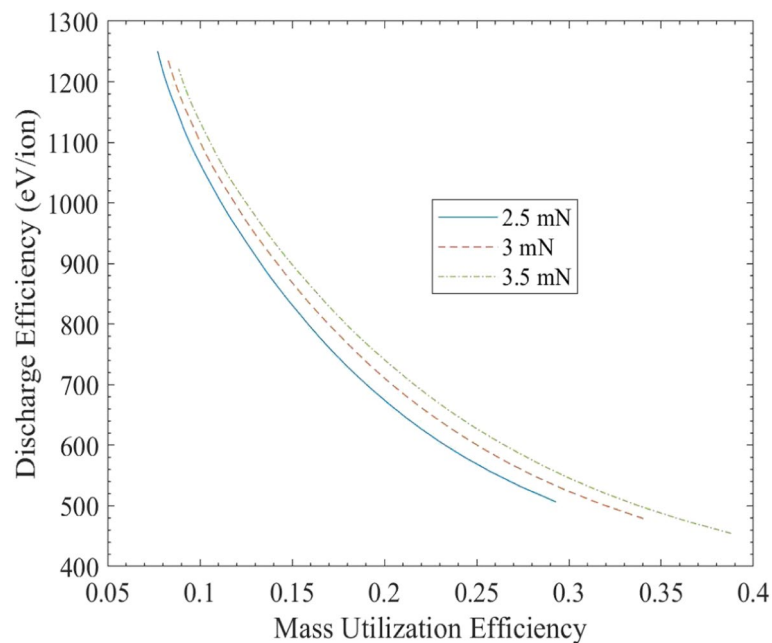


Fig. 11 Discharge efficiency versus mass utilization efficiency at constant thrust of 2.5 mN, 3 mN, and 3.5 mN. Results calculated at 150 km with moderate solar activity

at 150 km, the mass flow rate would increase to around 27 mg/s at 140 km and the required power for 3 mN of the thrust would increase by 3.5%. From Fig. 10, the change in mass flow rate due to a change in altitude would be more pronounced at lower altitudes within the range of 80 to 150 km.

In Fig. 11, the discharge efficiency decreases as the mass utilization efficiency increases in the range of mass flow rates considered. At 3 mN, the mass utilization efficiency at the optimal mass flow rate was approximately 0.15, while the corresponding discharge efficiency was approximately 870 eV/ion. The presented thruster is shown to be very inefficient, which indicates that the drag compensation capability of the thruster could improve significantly if the efficiencies are addressed. Design analysis of the plasma generation and the ion optics would be required to determine the possible improvement in the mass utilization and discharge efficiencies and how the thruster's drag compensation capability could improve.

It is suggested that the number of turns in the coil be increased to increase the axial magnetic field, as this would increase the ion confinement at a given RF power, which would subsequently increase the beam current and improve the discharge efficiency. In the design of the ion optics, it is recommended to achieve a higher ratio of the ion grid transparency to the neutral grid transparency, as this would increase the mass utilization efficiency.

The trend in Fig. 11 can be explained by noting how the influence of the intake mass flow rate affects the power balance and the mass utilization efficiency. From Eq. 18, it can be seen that for an increased intake mass flow rate, the neutral density in the discharge chamber must increase. Evaluating Eqs. 28, 29 and 30 shows that the RF power coupling increases at a slower rate than the neutral density. From Eq. 23 and noting that the floating sheath potential and the collision rates increase with electron temperature,

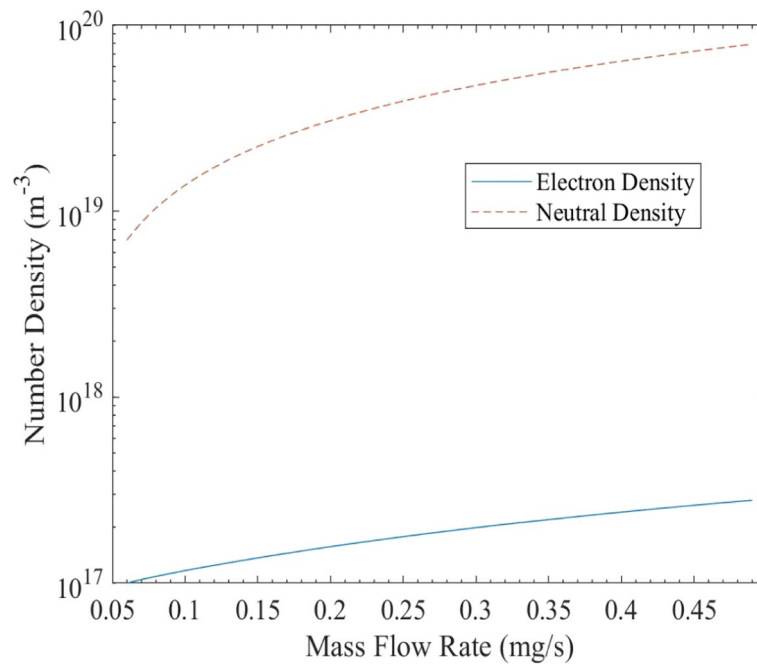


Fig. 12 Neutral and electron number densities versus mass flow rate at constant thrust of 3 mN. Results calculated at 150 km

as the power coupling increases slower than the neutral density, the electron temperature decreases to make up for the difference in energy. As the electron temperature decreases, the ionization fraction decreases, such that n_e/n_n decreases. The decrease in T_e and n_e/n_n decreases the mass utilization efficiency while also increasing the dominance of the excitation loss and ionization cost in Eq. 23; the increase in n_n/n_e then outweighs the decrease in T_e in Eq. 23, such that the discharge efficiency increases as the mass utilization decreases.

Over the range of mass flow rates modeled and for a net thrust of 3 mN, Fig. 12 shows that the electron density is between 10^{17} and $3 \times 10^{17} \text{ m}^{-3}$ and that the neutral density is between 7×10^{18} and $8 \times 10^{19} \text{ m}^{-3}$. It was observed that the change in neutral and electron density with altitude or solar activity was negligible. It is also seen that at low mass flow rates, the neutral density decreases faster than the electron density. The explanation for this trend follows the same reasoning as the analysis of Fig. 11. At low mass flow rates, the ionization fraction increases due to the decrease in the neutral density. The resultant increase in the ionization rates depletes the neutrals while increasing the electron density, and this effect is enhanced as the electron temperature keeps increasing at low mass flow rates.

In Fig. 13, the ion mole fractions are seen to follow a hyperbolic trend; this occurs because as the mass flow rate increases, there is a decrease in the electron temperature, which decreases the ionization fraction. At the low mass flow rates, the electron temperature is about 13 eV, while at the highest mass flow rates, the electron temperature was found to be around 6 eV. As an example of how this decrease in electron temperature affects the ionization rates, the ionization rate of N_2 shown in Fig. 5 decreases from $1.6 \times 10^{-14} \text{ m}^3/\text{s}$ to $2.2 \times 10^{-15} \text{ m}^3/\text{s}$ at 13 eV to 6 eV. At the lowest mass flow rate, the

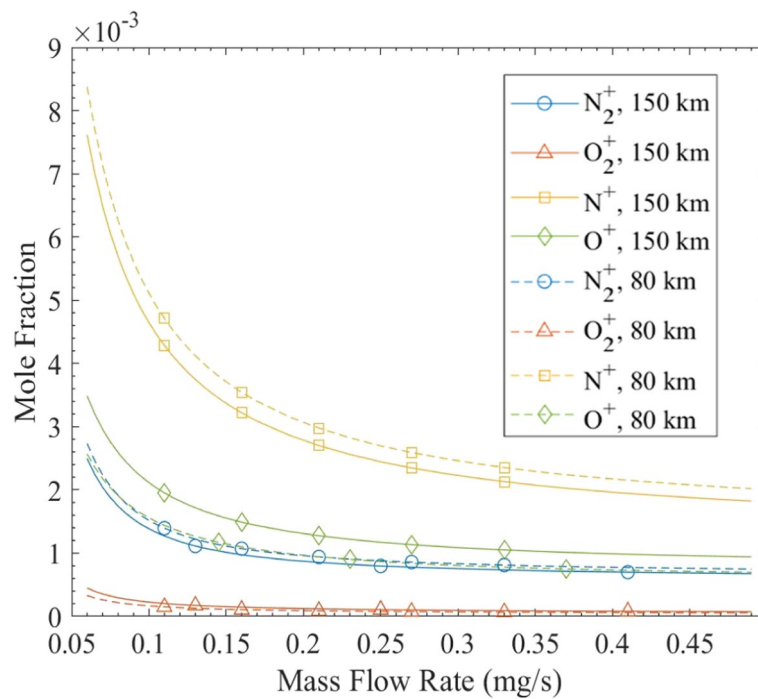


Fig. 13 Mole fractions of singly-charged ions versus mass flow rate at constant thrust of 3 mN. Results calculated at 150 km and 80 km

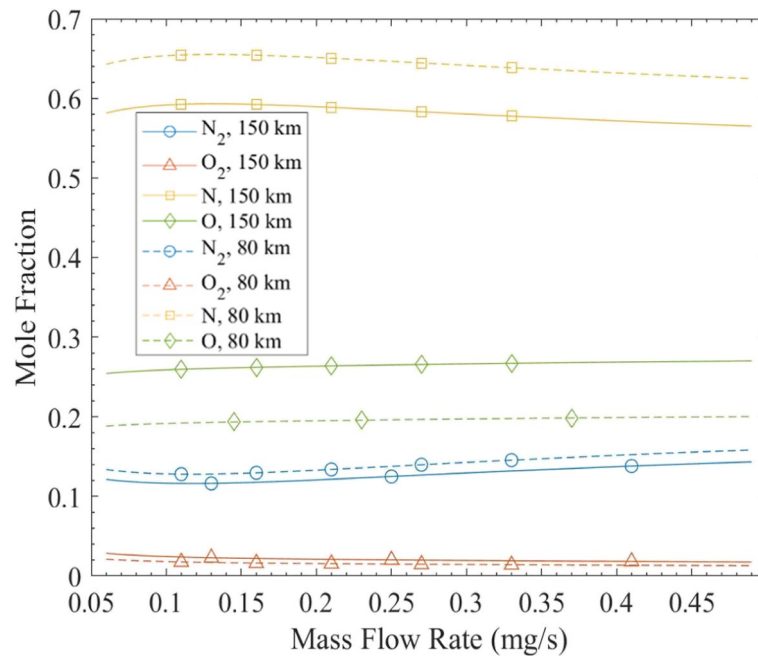


Fig. 14 Mole fractions of neutrals versus mass flow rate at constant thrust of 3 mN. Results calculated at 150 km and 80 km

total ionization fraction is around 1%, while at the optimal mass flow rate of 0.17 mg/s, the ionization fraction is around 0.5%.

The atomic ions have a higher density than their molecular counterparts, while at lower altitudes, N_2^+ and O^+ have similar densities. The fraction of oxygen ions that are molecules is smaller than that of nitrogen since at the range of electron temperatures considered, the dissociation rate of O_2 is 2-5 times larger than the ionization rate of O_2 , while the dissociation and ionization rates of N_2 are much closer to each other. The trends with a change in altitude are directly related to the change in composition shown in Fig. 4. The doubly-charged ions were found to have mole fractions two orders of magnitude less than the singly-charged ions; this is consistent with the small ionization fraction and the ionization rate of ions being an order of magnitude smaller than that of neutrals.

Similarly, in Fig. 14, the neutral atoms have a higher density than the neutral molecules, but the neutral mole fractions do not vary significantly with mass flow rate. The higher density of neutral atoms compared to that of neutral molecules agrees with the fact that neutral molecules are depleted due to both dissociation and ionization, while neutral atoms are only significantly depleted due to ionization. In the mass flow rate range considered, the neutral mole fractions of N_2 , O_2 , N , and O vary by approximately 0.03, 0.01, 0.03, and 0.02, respectively. The small change of the neutral mole fractions with mass flow rate occurs because the ratios of the dissociation rates to the ionization rates do not vary significantly in the resultant range of electron temperatures.

Regarding Figs. 13 and 14, the composition was also seen to vary with solar activity, but the variation in mole fractions was more pronounced with changes in altitude. This agrees with the change in the composition being more significant with a change in altitude than a change in solar activity. The large presence of N^+ and O^+ in the discharge chamber disagrees with [6], which suggested that N_2^+ and O_2^+ should be the most prominent ions in the discharge chamber. The significant presence of atomic oxygen in the discharge chamber indicates that thruster erosion needs to be examined in further studies. For a RIT, grid erosion is of primary concern, so it should be a focus in future studies of the presented thruster.

Conclusion

The validated composition and performance model presented in this paper can be used to predict the drag-compensation capability and discharge plasma composition of an air-breathing RIT. It should be noted that the presented model is applicable to altitudes higher than 150 km, but the scope of this article is limited to between 80 and 150 km, even though there are still challenges related to satellite operation at these low altitudes. It is concluded that the presented thruster is not capable of full drag compensation between 80 and 150 km due to the maximum net thrust of 3 mN at 1 kW of total input power. However, because the efficiencies at the optimal conditions are poor, it was suggested that a design analysis could improve drag compensation capabilities of the thruster. Specifically, it was suggested to increase the number of turns in the coil to increase the magnetic field and the beam current, as this would improve the thrust,

discharge efficiency, and mass utilization efficiency. It was also suggested to increase the size of the RIT to allow for efficient operation at larger mass flow rates. To further improve the drag compensation capability of the thruster, it is recommended to investigate the performance at an increased power. At the optimal conditions at 1 kW of total input power, the effect of solar activity only increased the required power by less than 1%; this indicates that the effects of solar activity should not be a focus of ABEP studies between 80 and 150 km. The high mole fractions of N , O , N^+ , and O^+ indicate that electron impact dissociation collisions are significant in the discharge chamber. Consequently, electron impact dissociation should be included in air-breathing models of all gridded ion thrusters, and the dominant presence of monatomic ions and atomic nitrogen and oxygen should be considered in experiments of any gridded ion thruster operating on an N_2/O_2 mixture. Although the presented thruster is predicted to only compensate for 2.85% of the drag on the reference satellite at 150 km, it is believed that an air-breathing RIT with a stronger magnetic field and a larger discharge chamber would provide significantly more drag compensation in VLEO, but the high presence of atomic oxygen in the discharge chamber emphasizes the need for a grid erosion study in order for an air-breathing RIT to be considered feasible.

Nomenclature

A_a	Back wall area
A_g	Grid area
A_w	Radial wall area
B	Magnetic field strength
e	elementary charge
E	Electric field
$f_{c,j}$	Confinement factor of the j^{th} ion
I_{coil}	Time-averaged current through the coil
k	Wavenumber
k_B	Boltzmann constant
K	Collision rate
\dot{m}_n	Mass flow rate of inlet gas
m_n	Average mass of an air molecule at the inlet
\dot{m}_0	Mass flow rate at the intake
n_e	Electron number density
$n_{i,j}$	Number density of j^{th} ion
$n_{n,k}$	Number density of k^{th} neutral
P_{abs}	Power absorbed by the discharge plasma
P_{loss}	Power exiting the discharge chamber
q_j	Charge of j^{th} ion
Q	Particle flux or particle production rate
R	Discharge chamber radius
R_{coil}	Coil resistance
T_e	Electron temperature (K)
T_g	Ion grid transparency
$T_{g,n}$	Neutral grid transparency

- U_{ek}^{xp} Threshold potential of the corresponding inelastic process
 $v_{B,j}$ Bohm velocity of the j^{th} ion
 v_e Electron velocity
 $v_{n,k}$ Thermal velocity of k^{th} neutral
 $x_{i,k}$ Mole fraction of k^{th} neutral at thruster inlet
 ε_0 Vacuum permittivity
 $\ln \Lambda_j$ Coulomb logarithm
 μ_0 Vacuum permeability
 μ_e Electron mobility
 η_c Clausing factor
 ν_m Electron elastic momentum transfer collision frequency
 σ Collision cross-section
 Φ Floating sheath potential
 ω Driving frequency

Appendix

Following Goebel's derivation of the confinement factor in [14] and accounting for multiple ion species:

$$v_e \left(1 + \mu_e^2 B^2\right) = \mu_e \left(E + \frac{k_B T_e}{e} \frac{\nabla n}{n}\right) + \frac{\sum_j v_{ei,j}^{el} v_{ij}}{v_m}. \quad (\text{A-1})$$

The electron velocity can be substituted using ambipolar flow, such that

$$v_e = \frac{\sum_j n_{ij} q_j v_{ij}}{n_e e}. \quad (\text{A-2})$$

Because ambipolar flow is assumed, the inelastic collision rates are neglected near the radial wall edge. Combining Eqs. A-1 and A-2,

$$\frac{\sum_j n_{ij} q_j v_{ij}}{n_e e} \left(1 + \mu_e^2 B^2\right) = \mu_e \left(E + \frac{k_B T_e}{eR}\right) + \frac{\sum_j v_{ei,j}^{el} v_{ij}}{v_m} \quad (\text{A-3})$$

where $\nabla n/n$ is approximated as $1/R$. It is necessary to relate the velocities of the different ions in order to solve for the velocity of each ion species. From ion conservation of a given species, the ion loss at the radial wall is given by

$$Q_{w,j} = Q_{p,j} - Q_{s,j} - Q_{b,j} - Q_{a,j} \equiv Q_{net,j}. \quad (\text{A-4})$$

The ion loss at the radial wall for a given species is also given by

$$Q_{w,j} = n_{i,j} v_{i,j} A_w \quad (\text{A-5})$$

such that for two ion species, their velocities are related by

$$\frac{v_{i,j}}{v_{i,k}} = \frac{Q_{net,j}}{Q_{net,k}} \frac{n_{i,k}}{n_{i,j}} \equiv \alpha_{jk}. \quad (\text{A-6})$$

Substituting Eq. A-6 into Eq. A-3,

$$v_{i,j} \sum_k \frac{n_{i,k} q_k \alpha_{jk}}{n_e e} (1 + \mu_e^2 B^2) = \mu_e \left(E + \frac{k_B T_e}{eR} \right) + v_{i,j} \sum_k \frac{v_{ei,k}^{el} \alpha_{jk}}{v_m}. \quad (\text{A-7})$$

For $v_{i,j}$ to equal $v_{B,j}$ in the limit of no magnetic field and negligible collisions, it can be seen that at the plasma-edge region for a specific ion, the transverse electric field must have a maximum of

$$E_j = -\frac{m_{i,j} v_{i,j}^2}{q_j R}. \quad (\text{A-8})$$

Substituting Eq. A-8 into Eq. A-7 and letting $A_{j,1} = \sum_k \frac{n_{i,k} q_k \alpha_{jk}}{n_e e}$ and $A_{j,2} = \sum_k \frac{v_{ei,k}^{el} \alpha_{jk}}{v_m}$, Eq. A-7 can be rearranged into

$$v_{i,j}^2 + \frac{q_j R}{\mu_e m_{i,j}} [A_{j,1} (1 + \mu_e^2 B^2) - A_{j,2}] v_{i,j} - \frac{k_B T_e q_j}{m_{i,j} e} = 0 \quad (\text{A-9})$$

The velocity at the plasma edge for a specific ion is then

$$v_{i,j} = \frac{1}{2} \sqrt{\left[\frac{q_j R}{\mu_e m_{i,j}} [A_{j,1} (1 + \mu_e^2 B^2) - A_{j,2}] \right]^2 + \frac{4 k_B T_e q_j}{m_{i,j} e}} - \left[\frac{q_j R}{2 \mu_e m_{i,j}} [A_{j,1} (1 + \mu_e^2 B^2) - A_{j,2}] \right] \quad (\text{A-10})$$

Acknowledgements

The authors would like to thank Gianluca Cifali for providing experimental data and Maria Smirnova for proving experimental conditions that were used to validate the presented model.

Code availability

Code is available upon request to the authors.

Authors' contributions

J. Lopez-Uricoechea and M. L. R. Walker contributed to the study conception and design. Material preparation, data collection and analysis were performed by J. Lopez-Uricoechea, and data interpretation was performed by J. Lopez-Uricoechea and D. Lev. All authors contributed to the model development. The first draft of the manuscript was written by J. Lopez-Uricoechea, and all authors commented on previous versions of the manuscript. All authors read and approved the final manuscript.

Funding

No funding was received for conducting this study.

Availability of data and materials

Data are available upon request to the authors.

Declarations

Competing interests

The authors have no competing interests that are relevant to the content of this article.

Received: 20 April 2022 Accepted: 8 September 2022

Published online: 26 September 2022

References

1. Crisp NH, Roberts PCE, Livadiotti S et al (2020) The benefits of very low earth orbit for earth observation missions. *Prog Aerosp Sci* 117:100619. <https://doi.org/10.1016/j.paerosci.2020.100619>
2. Hruby V, Pote B, Bogan T, et al (2003) U.S. Patent Application for Air Breathing Electrically Powered Hall Effect Thruster. Docket No. US 683492 B2, filed 21 June 2002.
3. Goebel DM, Katz I (2008) Fundamentals of Electric Propulsion: Ion and Hall Thrusters. *Jet Prop Lab*. <https://doi.org/10.1002/9780470436448>

4. Romano F, Espinosa-Orozco J, Pfeiffer M et al (2021) Intake design for an Atmosphere-Breathing Electric Propulsion System (ABEP). *Acta Astronaut* 187:225–235. <https://doi.org/10.1016/j.actaastro.2021.06.033>
5. Nishiyama K (2003) Air Breathing Ion Engine Concept. *Proc 54th Int Astronaut Congr IAC-03-S4-02*. <https://doi.org/10.2514/6.JAC-03-S.4.02>
6. Tagawa M, Yokota K, Nishiyama K et al (2013) Experimental Study of Air Breathing Ion Engine Using Laser Detonation Beam Source. *J Propuls Power* 29(3):501–506. <https://doi.org/10.2514/1.B34530>
7. Di Cara D, Gonzalez del Amo J, Santovincenzo A, et al (2007) RAM Electric Propulsion for Low Earth Orbit Operation: an ESA study. In: *Proceedings of the 30th International Electric Propulsion Conference (IEPC Paper 2007–162)*. Electric Rocket Propulsion Society, Florence.
8. Cifali G, Dignani D, Misuri T, et al (2012) Completion of HET and RIT characterization with atmospheric propellants. In: *Proceedings of the 2012 Space Propuls Conf, Bordeaux (Space Propul Conf Paper SP2012_2355386)*.
9. Andreussi T, Cifali G, Giannetti V, et al (2017) Development and Experimental Validation of a Hall Effect Thruster RAM-EP Concept. In: *Proceedings of the 35th International Electric Propulsion Conference (IEPC Paper 2017–377)*. Electric Rocket Propulsion Society, Atlanta.
10. Shabselowitz A (2013) *Study of RF Plasma Technology Applied to Air-Breathing Electric Propulsion*. PhD thesis, University of Michigan.
11. Garrigues L (2012) Computational Study of Hall-Effect Thruster with Ambient Atmospheric Gas as Propellant. *J Propuls Power* 28(2):344–354. <https://doi.org/10.2514/1.B34307>
12. Romano F, Chan Y-A, Herdrich G et al (2020) RF Helicon-based Inductive Plasma Thruster (IPT) Design for an Atmosphere-Breathing Electric Propulsion system (ABEP). *Acta Astronaut* 176:476–483. <https://doi.org/10.1016/j.actaastro.2020.07.008>
13. Pekker L, Keidar M (2012) Analysis of Airbreathing Hall-Effect Thrusters. *J Propuls Power* 28(6):1399–1405. <https://doi.org/10.2514/1.B34441>
14. Goebel DM (2008) Analytical Discharge Model for RF Ion Thrusters. *IEEE Trans Plasma Sci* 36(5):2111–2121. <https://doi.org/10.1109/TPS.2008.2004232>
15. Chabert P, Braithwaite N (2011) *Inductively Coupled Plasmas*. In: *Physics of Radio-Frequency Plasmas*. Cambridge University Press, pp. 219–259. <https://doi.org/10.1017/CBO9780511974342>
16. Singh LA (2014) *Very Low Earth Orbit Propellant Collection Feasibility Assessment*. PhD thesis, Georgia Institute of Technology.
17. Diamant KD (2010) A 2-Stage Cylindrical Hall Thruster for Air Breathing Electric Propulsion. In: *Proceedings of the 46th AIAA/ASME/SAE/ASEE Jt Propuls Conf Exhib, Nashville (AIAA Paper 2010–6522)*. <https://doi.org/10.2514/6.2010-6522>
18. Picone JM, Hedin AE, Drob DP, Aikin AC (2002) NRLMSISE-00 empirical model of the atmosphere: Statistical comparisons and scientific issues. *J Geophys Res* 107(A12):1468–1483. <https://doi.org/10.1029/2002JA009430>
19. (2008) ECSS-E-ST-10-04C – Space environment. *Eur Coop Space Stand. ESA Requir Stand Div, Noordwijk*.
20. Kossyi IA, Kostinsky AY, Matveyev AA, Silakov VP (1992) Kinetic scheme of the non-equilibrium discharge in nitrogen – oxygen mixtures. *Plasma Sources Sci Technol* 1(3):207–220. <https://doi.org/10.1088/0963-0252/1/3/011>
21. Itikawa Y (2006) Cross Sections for Electron Collisions with Nitrogen Molecules. *J Phys Chem Ref Data* 35(31):31–53. <https://doi.org/10.1063/1.1937426>
22. Itikawa Y (2009) Cross Sections for Electron Collisions with Oxygen Molecules. *J Phys Chem Ref Data* 38(1):1–20. <https://doi.org/10.1063/1.3025886>
23. Krishnakumar E, Srivastava SK (1991) Cross-sections for electron impact ionization of O₂. *Int J Mass Spectrom and Ion Process* 113(1):1–12. [https://doi.org/10.1016/0168-1176\(92\)87037-F](https://doi.org/10.1016/0168-1176(92)87037-F)
24. Brook E, Harrison MFA, Smith ACH (1978) Measurements of the electron impact ionisation cross sections of He, C, O, and N atoms. *J Phys B: Atom Mol Phys* 11(17):3115–3132. <https://doi.org/10.1088/0022-3700/11/17/021>
25. Laher RR, Gilmore FR (1990) Updated Excitation and Ionization Cross Sections for Electron Impact on Atomic Oxygen. *J Phys Chem Ref Data* 19:277–305. <https://doi.org/10.1063/1.555872>
26. Harrison MFA, Dolder KT, Thonemann PC (1963) A Measurement of the Cross Section for the Ionization of N⁺ to N²⁺ by Electron Impact. *Proc Phys Soc* 82:368–371. <https://doi.org/10.1088/0370-1328/82/3/305>
27. Aitken KL, Harrison MFA (1971) Measurement of the cross sections for electron impact ionization of multi-electron ions I. O⁺ to O₂⁺ and O₂⁺ to O₃⁺. *J Phys B Atom Mol Phys* 4(9):1176–1188. <https://doi.org/10.1088/0022-3700/4/9/007>
28. Bahati EM, Jureta JJ, Belic DS, Cherkani-Hassani H et al (2001) Electron impact dissociation and ionization of N₂⁺. *J Phys B: Atom Mol Opt Phys* 34(15):2963–2973. <https://doi.org/10.1088/0953-4075/34/15/303>
29. Cherkani-Hassani H, Belic DS, Jureta JJ, Defrance P (2006) Absolute cross sections for electron impact ionization and dissociation of O₂⁺. *J Phys B Atom Mol Opt Phys* 39(24):5105–5117. <https://doi.org/10.1088/0953-4075/39/24/008>
30. Alves LL, Coche P, Ridenti MA, Guerra V (2016) Electron scattering cross sections for the modelling of oxygen-containing plasmas. *Eur Phys J D* 70:124–132. <https://doi.org/10.1140/epjd/e2016-70102-1>
31. Tayal SS, Zatsarinny O (2005) *B-spline and R-matrix with pseudostates approach for electron impact excitation of atomic nitrogen*. *J Phys B: Atom Mol Opt Phys* 38(20):3631–3645. <https://doi.org/10.1088/0953-4075/38/20/001>
32. Cosby PC (1993) Electron-impact dissociation of nitrogen. *J Chem Phys* 98:9544–9553. <https://doi.org/10.1063/1.464385>
33. Cosby PC (1993) Electron-impact dissociation of oxygen. *J Chem Phys* 98:9560–9569. <https://doi.org/10.1063/1.464387>
34. Wang Y, Zatsarinny O, Bartschat K (2014) *B-spline and R-matrix-with-pseudostates calculations for electron-impact excitation and ionization of nitrogen*. *Phys Rev A* 89(6):2714–2725. <https://doi.org/10.1103/PhysRevA.89.062714>
35. Vojnovic M, Popovic M, Ristic MM et al (2015) Rate coefficients for electron impact excitation of N₂. *J Chem Phys* 143:38–46. <https://doi.org/10.1016/j.chemphys.2015.09.014>
36. Cartwright DC (1978) Rate coefficients and inelastic momentum transfer cross sections for electron excitation of N₂ by electrons. *J Appl Phys* 49:3855–3862. <https://doi.org/10.1063/1.325390>

37. Goldston RJ, Rutherford PH (1995) Collisions in fully ionized plasmas. In: *Introduction to Plasma Physics*. Institute of Physics Publishing, Bristol, pp. 147–164.
38. Godyak VA (1986) Spatial Distribution of RF Discharge Plasmas. In: *Soviet Radio Frequency Discharge Research*. Delphic Associates, Falls Church, pp. 79–102.